Chemistry Europe
European Chemical Societies Publishing

WILEY VCH

Excellence in Chemistry Research

Announcing our new flagship journal

- Gold Open Access
- Publishing charges waived
- Preprints welcome
- Edited by active scientists

Meet the Editors of *ChemistryEurope*

Luisa De Cola
Università degli Studi di Milano Statale, Italy

Ive Hermans
University of Wisconsin-Madison, USA

Ken Tanaka
Tokyo Institute of Technology, Japan

ChemCatChem

Research Article
doi.org/10.1002/cctc.202300792

Chemistry Europe
European Chemical Societies Publishing

www.chemcatchem.org

Oxide-derived Silver Nanowires for CO_2 Electrocatalytic Reduction to CO

Francesco Mattarozzi,[a] Nolan van der Willige,[a] Valerio Gulino,[a] Claudia Keijzer,[a] Rim C. J. van de Poll,[b] Emiel J. M. Hensen,[b] Peter Ngene,[a] and Petra E. de Jongh*[a]

Silver electrocatalysts offer the possibility to produce CO by converting CO_2, enabling the use of a greenhouse gas as chemical building block. Compared to nanoparticles, silver nanowires show an enhanced selectivity towards CO. Recent publications proved that oxide-derived electrocatalysts can exhibit better catalytic performance than the pristine metal phase, but oxide-derived silver nanowires have not been investigated. In this work, we report for the first time the electrocatalytic properties of silver nanowires, synthesized via the polyol method, and pretreated by electrochemical oxidation in basic electrolyte. By increasing the oxidation potential, both the percentage of Ag_xO and the surface roughness of the catalyst were progressively increased. The most oxidized sample showed a remarkably improved CO selectivity ($-294.2\ mA\ m^{-2}_{Ag}$), producing a 3.3-fold larger CO partial current density than the pristine sample ($-89.4\ mA\ m^{-2}_{Ag}$), normalized by electrochemically active silver surface area. This work demonstrates the beneficial effect of the controlled oxidation treatment even on highly selective nanostructures such as silver nanowires.

Introduction

The implementation of CO_2 capture and utilization would enable the use CO_2 as a valuable feedstock.[1–3] The electrochemical conversion of CO_2 is a particularly exciting prospect. Pioneered by Hori in the late 90s,[4] the interest around this technology is nowadays revived,[5,6] thanks to the decreasing cost of renewable electricity.[7] CO_2 electrochemical reduction (often referred to as "CO_2 Reduction Reaction" or "CO_2RR") involves multiple proton and electron transfer processes, generating C_1/C_2 products, such as CO, HCOOH, CH_4, C_2H_4,[8,9] and recently small concentrations of up to C_6 products.[10] The water/proton reduction (namely Hydrogen Evolution Reaction (HER)) is the main competing reaction and lowers the selectivity of the process. Therefore, the choice of suitable electrocatalysts is key to steer the selectivity of the process towards the desired product(s).[11,12]

Silver is a selective catalyst to convert CO_2 and produce CO, which can be utilized as building block for a wide range of chemicals, such as acetic acid,[13] methanol and long-chain hydrocarbons via the Fischer-Tropsch process.[14] The selectivity towards CO is due to the surface properties of silver, which enable the first electron transfer to CO_2 and the subsequent formation of the first reaction intermediate (*COO^-), which often constitutes the rate determining step for this electrochemical reaction, with a moderate binding energy. After a first proton transfer generating *COOH, a second proton and electron transfer lead to the formation of a *CO intermediate, bound to the surface with a low binding energy, and hence rapidly desorbing.[15,16] Several research groups have focused their attention on different silver nanostructures, such as nanoparticles,[17] nanoporous electrodes[18] and surface modified nanofoams,[19] aiming to enhance the catalytic performance.

Silver nanowires perform remarkably well catalytically compared to polycrystalline electrodes and nanoparticles.[20–22] For instance, it was shown that nanowires (100 nm in diameter) produced a higher selectivity (up to 70% faradaic efficiency) towards CO compared to polycrystalline nanoparticles (40% faradaic efficiency), at relatively modest overpotential (*i.e.* −1.2 V vs RHE). This was attributed to the high (100) to (111) facet ratio and edge to corner ratio in the 1-D nanostructure, which lowers the activation energy for the rate determining step of the reaction (first electron transfer to CO_2), as shown by DFT calculations.[23] Furthermore, nanowires possess high surface area and are suitable for surface modifications, as common synthesis procedures, such as the polyol method, aim to generate relatively thick nanowires (25 nm < diameter < 100 nm). For instance, the structure of silver nanowires was modified via wet-chemical sulfidation, introducing surface defects after the stripping of the sulfur atoms.[24] Although the surface roughening modified part of the original crystalline structure, it also formed active sites that led to a 20% increase in CO faradaic efficiency compared to the pristine wires (50% CO

[a] F. Mattarozzi, N. van der Willige, Dr. V. Gulino, C. Keijzer, Dr. P. Ngene, Prof. Dr. P. E. de Jongh
Material Chemistry and Catalysis
Debye Institute for Nanomaterials Science
Utrecht University
Universiteitsweg 99
3584 CG Utrecht (The Netherlands)
E-mail: p.e.dejongh@uu.nl

[b] R. C. J. van de Poll, Prof. Dr. E. J. M. Hensen
Laboratory of Inorganic Materials and Catalysis
Department of Chemical Engineering and Chemistry
Eindhoven University of Technology
P.O. Box 513
5600 MB Eindhoven (The Netherlands)

Supporting information for this article is available on the WWW under https://doi.org/10.1002/cctc.202300792

faradaic efficiency) at −0.9 V. However, the sulfidation treatment involves a complicated chemical step, implies the use of additional chemicals and the risk of H_2S evolution.

A similar approach to enhance the electrochemical performance of transition metal electrodes, involves the oxidation and subsequent reduction.[25,26] For instance, it has been demonstrated that an oxide-derived (OD-) nanoporous gold electrode, produced by electrochemical dealloying of a gold-silver foil in nitric acid, produced a larger CO partial current density than a pristine nanoporous gold electrode, with $-20\ mA\,cm^{-2}$ and $-7\ mA\,cm^{-2}$, respectively.[27] Seemingly, oxide-derived gold particles, obtained by pulse anodization of a pure gold electrode, achieved nearly full CO selectivity (>96%) at low overpotentials (−0.35 V), where the polycrystalline electrode was inactive towards the CO_2RR under these conditions.[25] Electrokinetic studies indicated that the CO_2RR was limited by the first electron transfer to CO_2 on polycrystalline gold electrode, while the subsequent proton transfer was the rate determining step for oxide-derived gold particles. Kanan *et al.*[28] observed a similar catalytic behavior for oxide-derived copper electrodes, obtained via thermal annealing of copper foils. The selectivity towards CO increased (up to 40% at −0.5 V) with increasing thickness of the surface oxide layer (Cu_2O – before cathodic condition were applied), tuned by changing the annealing temperature. Another study demonstrated that the maximum in ethylene and ethanol faradaic efficiency (34% and 16% at −0.99 V, respectively) was achieved by a catalyst with 3.6 μm galvanostatically deposited Cu_2O layer (pre-catalysis) and subsequently reduced to Cu^0, while the pure copper electrode only generated 13% and 0% faradaic efficiencies at the same potentials.[29]

Commonly, plasma treatments, thermal annealing in air or anodic pulses are used to modify silver electrodes, which are subsequently reduced electrochemically. Oxide-derived silver electrodes outperform pristine silver by increasing CO production and suppressing the hydrogen evolution. For instance, electrochemical oxidation (by pulse anodization) of a polycrystalline bulk silver electrode led to a large increase in CO selectivity, up to 75% at only −0.6 V, although it has to be noted that the pristine electrode showed a very poor selectivity (less than 5%) at the same potential.[30] The same strategy was applied on nanostructured materials, such as nanoparticles.[31] The origin of the improved performance for oxide-derived silver electrodes is still under debate. Using grazing angle EXAFS,[32] the enhanced CO selectivity was correlated to the presence of sub-surface oxygen atoms after the reduction step, and it was postulated that this led to a higher stability of $*COO^-$ reaction intermediate compared to the pure silver surfaces. Another study suggested that CO_2 interacted with Ag surfaces generating a carbonic acid-like intermediate, $O{=}CO_2^{\delta-}$, which led to an enhanced selectivity towards CO.[33] Other groups ascribed the change in selectivity to change in local pH, influenced by the increased surface roughness and porosity compared to flat silver foils.[30] It has also been suggested that the low coordination number of silver atoms[34] or the massive presence of defects[35] at the surface of oxide-derived materials, after stripping off the oxygen atoms, might influence the electrocatalytic performance of OD-electrodes.

In this work, we applied an electrochemical oxidation treatment on supported silver nanowires for the first time, to further enhance the catalytic properties of this very selective silver nanostructure. We were able to control and quantify the oxidation state of silver nanowires and we systematically followed the change in morphology as a function of the oxidation potential. Finally, we correlated the change in morphology and oxidation degree to the enhanced catalytic performance of the oxide-derived silver nanowires, leading to remarkably high selectivity towards CO compared to the pristine nanowires.

Results and Discussion

Synthesis and characterization of oxide-derived silver nanowires

Figure 1 shows transmission electron microscopy (TEM) images of nanowires synthesized via the polyol method. The average diameter of the wires was 61 ± 17 nm (inset, Figure 1b) and the average length was 10 μm, leading to an aspect ratio of around 160. The epitaxial growth of the nanowires is due to the strong poly(vinyl)-pyrrolidone adsorption preferentially on the (100) facets of the silver seeds,[36,37] which directs the addition of silver atoms onto the uncapped (111) facets, generating 1-D nanostructures. The right frame of Figure 1 shows the faceting at the tip of the nanowires, formed by the intersection between the (100) plane and the (111) plane. The formation of the nanowires was qualitatively followed via UV-vis measurements. Two absorption bands are observed at 350 nm and 377 nm, corresponding to the wire's surface plasmon resonance absorption bands (Figure S1).[38] The pristine nanowires were used as a starting point to study the influence of different oxidation treatments on the oxidation state, morphology, and catalytic performance of the silver nanowires.

Figure 2a displays the current evolution as a function of the applied anodic potential, obtained via linear sweep voltamme-

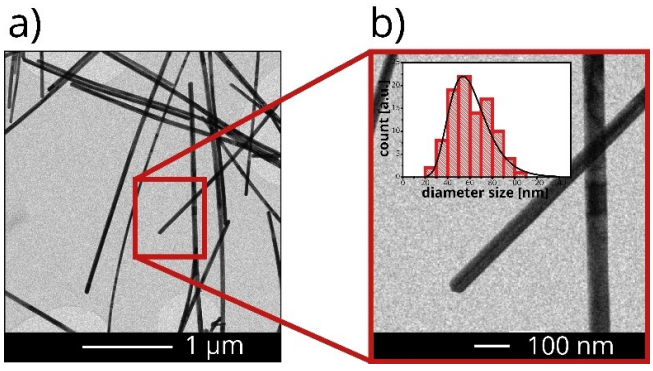

Figure 1. a) Transmission electron micrographs of silver nanowires synthesized via the polyol method, b) high magnification of two nanowires. The inset in Figure 1b shows the size distribution of the diameter of the as-synthesized silver nanowires.

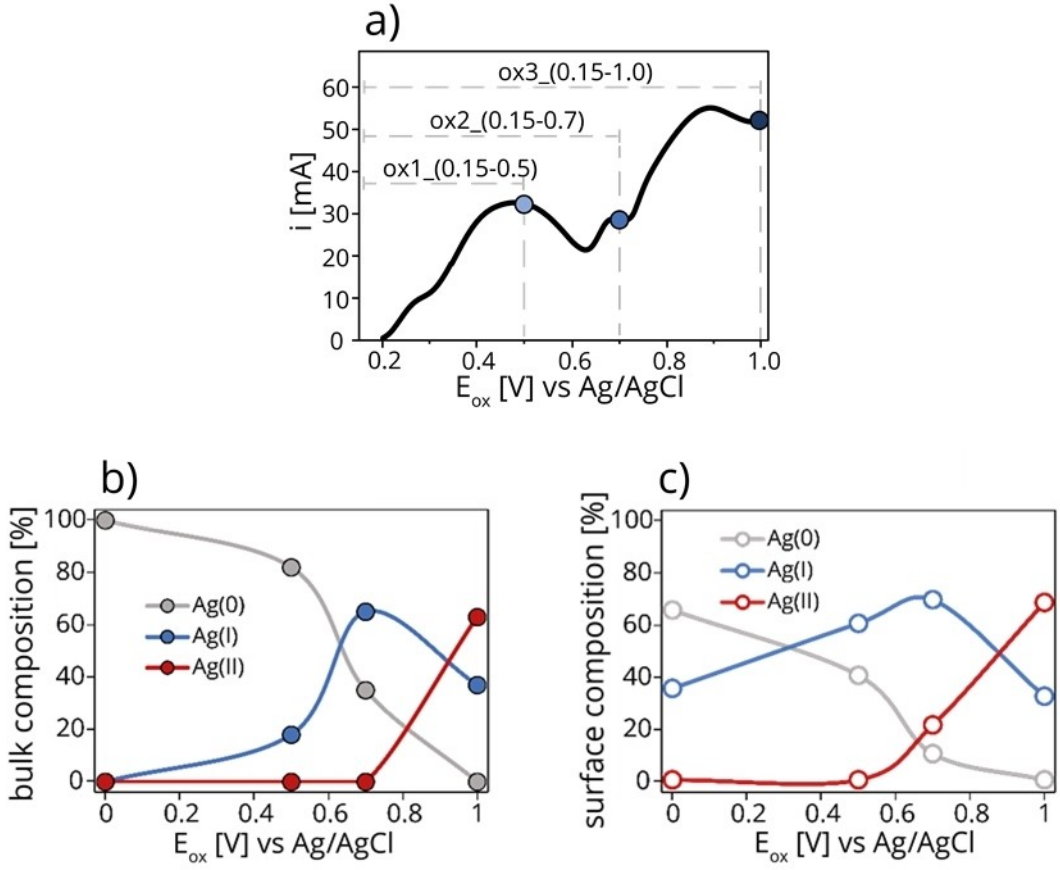

Figure 2. a) Current versus voltage curves measured in 0.2 M NaOH at 10 mV s^{-1} showing an anodic current due to the electrochemical oxidation of the silver nanowires. The composition of the different silver oxidation states was measured b) in the nanowires bulk by XRD and c) at the nanowires surface by XPS, for pristine, ox1, ox2 and ox3 catalysts. The samples were analyzed after the oxidation treatment.

try performed in 0.2 M NaOH at 10 mV s^{-1}. Two main peaks were detected: the first peak, ranging from +0.2 V to +0.63 V, is assigned to the oxidation of silver to silver(I) oxide (equation 1), while the second peak, centered at +0.9 V, is attributed to further oxidation of silver(I) oxide to silver(II) oxide (equation 2):

$$Ag_2O(s) + H_2O(aq) + 2e^- \leftrightharpoons 2Ag\ (s) + 2OH^-(l)\ E^0_{Ag_2O/Ag} = 0.342\ V \quad (1)$$

$$2AgO(s) + H_2O(aq) + 2e^- \leftrightharpoons Ag_2O(s) + 2OH^-(l)\ E^0_{AgO/Ag_2O} = 0.602\ V \quad (2)$$

Where $E^0_{Ag2O/Ag}$ and $E^0_{AgO/Ag}$ are the reduction potentials of the reactions versus standard hydrogen potential. This electrochemical procedure allowed control over the oxidation degree of the nanowires, by setting a maximum oxidation potential, producing three different catalysts: ox1 (0.15–0.5) partially oxidized to Ag_2O, ox2 (0.15–0.7) with extensive oxidation to Ag_2O, and ox3 (0.15–1.0) almost completely oxidized to AgO, as highlighted by the current peak deconvolution and integration (Figure S2) and indicated by the blue dots in Figure 2a.

After the oxidation treatment, we ex-situ characterized the oxidation state of the silver nanowires with XRD (bulk analysis) and XPS (surface analysis). Quantitative Rietveld refinement analysis of the XRD raw data (Figure S3, outcome presented in Figure 2b revealed that, starting from completely metallic silver in the pristine nanowires (0 V oxidation potential), about 18% (wt/wt) of the silver was in the form of Ag_2O after oxidation up to 0.5 V. By further oxidation up to 0.7 V, the percentage of Ag_2O increased to 65%. Extending to the most positive oxidation potential (1.0 V vs Ag/AgCl), the nanowires consisted of 66% AgO and 34% Ag_2O, while no metallic silver was left.

Figure 2c shows the XPS analysis derived from the deconvolution of the two silver peaks, generated by the spin orbit splitting of the 3d electrons (Figure S4).[39] The surface analysis (approximately 2 nm) demonstrated that the pristine silver nanowires had a passivation surface layer (due to the exposure to air) that was not detected by the XRD measurement. The ox1 (0.15–0.5) catalyst surface consisted of about 60% Ag_2O and 40% metallic silver, while ox2 (0.15–0.7) contained 20% (wt/wt) AgO, not detected in the XRD measurement. Finally, ox3 (0.15–1.0) showed only AgO and Ag_2O.

A comparison between the bulk (Figure 2b and surface composition (Figure 2c demonstrates that, although both analyses show a similar trend, the percentage of oxide at the surface (Figure 2c, XPS) was larger than in the bulk (Figure 2b, XRD). This is logical as oxidation took place at the interface between the nanowires and the basic electrolyte, where the oxygen was introduced into the silver crystal lattice. By increasing the bias, subsurface layers started to get oxidized, and the oxidation process penetrated towards the core of the nanowires.[40,41] All samples, after oxidation treatment, were reduced by scanning from 0.15 V to −1.0 V vs Ag/AgCl in 0.1 M $KHCO_3$ with 10 mV s^{-1}. This led to reduction to metallic silver, and these samples from now on are denoted as oxide-derived (OD-) Ag nanowires.

The morphology of the pristine and OD-nanowires was studied by scanning electron microscopy (SEM). Figure 3 shows representative images, acquired both at lower magnification (top row) and higher magnification (bottom row) to analyze the morphology at nanoscale. The low magnification images show that after oxidation and reduction treatment the remaining nanowires were located close to the ca. 10 μm diameter carbon paper fibers. By increasing the oxidation potential, the underlying nanowire architecture is preserved, but the shape of the nanowires becomes more irregular, illustrated by the ox2 (0.15–0.7) sample. By further increasing the oxidation potential to 1.0 V, the features became less sharp and defined, though still resembling the original nanowires morphology. Furthermore, while the density of nanowires on the carbon paper decreased upon oxidation, the thickness of the nanostructure increased.

Electrocatalytic activity and selectivity

The electrocatalytic performance of the oxide-derived (OD)-nanowires was compared with that of the pristine catalyst. Figure 4a displays the electrochemical current density of the during cycling performed in 0.1 M $KHCO_3$. All the OD-catalysts produced a slightly larger current density than the pristine nanowires when normalized per geometric surface area. ox2 (0.15–0.7) produced the largest current density, possibly due to its high surface roughness. The OD-catalyst had a lower onset potential than the pristine nanowires. The same trend was observed during chronoamperometry measurements (Figure S5), where each data point corresponds to the average total current density over 30 minutes of analysis.

Impedance spectra were recorded for the pristine and ox3 (0.15–1.0) samples at each potential, to assess the difference in charge transfer resistance between the as-synthesized and most oxidized catalysts (Figure 4b). The inset in Figure 4b, shows the equivalent circuit used to fit the impedance raw data, corresponding to a simple resistance-constant phase element-resistance circuit (Randles circuit).[42] R_{el} is the electrolyte resistance, while R_{ct} is the charge transfer resistance, which corresponds to the intrinsic resistance to the electron transfer occurring at the interface of the catalyst. The OD-catalyst showed a lower charge transfer resistance than the pristine sample through the entire potential range. The difference between the two electrodes is small at low potentials (−0.6 V), where they both showed a relatively small current density and a large resistance, with 63 ohm and 59 ohm for pristine and oxidized sample respectively. At larger potentials (−0.9 V and −1.4 V), the difference was larger, with the pristine nanowires

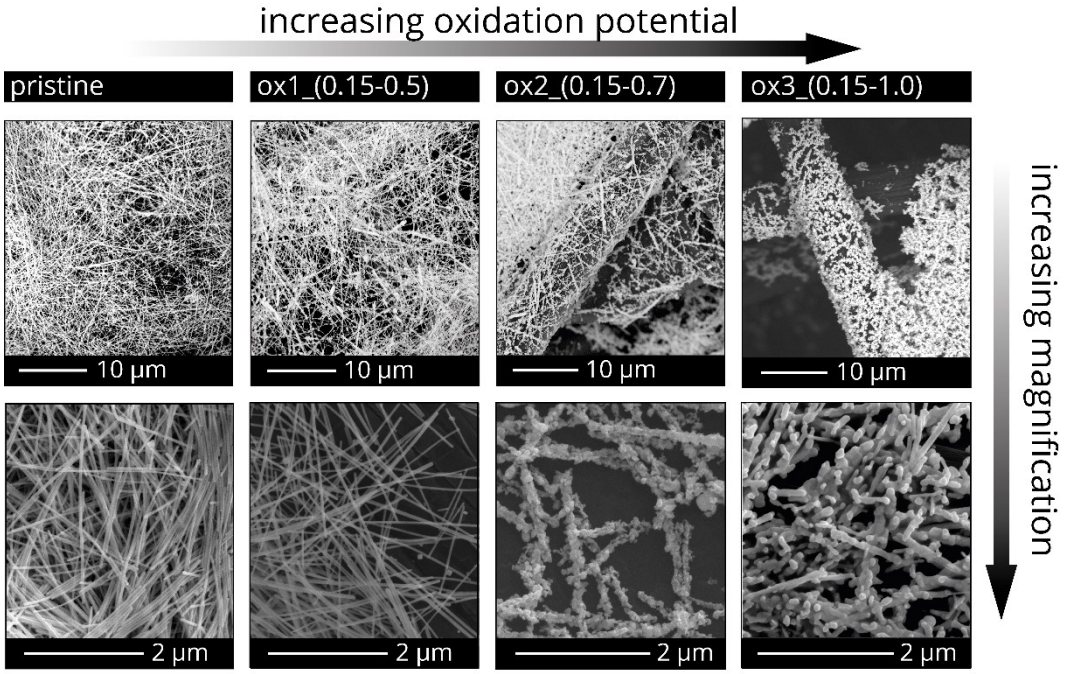

Figure 3. Scanning electron micrographs (SEM) of silver nanowires both pristine (left) and OD-nanowires after exposure to different oxidation potentials followed by reduction at −1.0 V (right). The top row shows the dispersion of nanowires on the carbon paper (low magnification). The bottom row shows the morphology of the nanowires in more detail (high magnification).

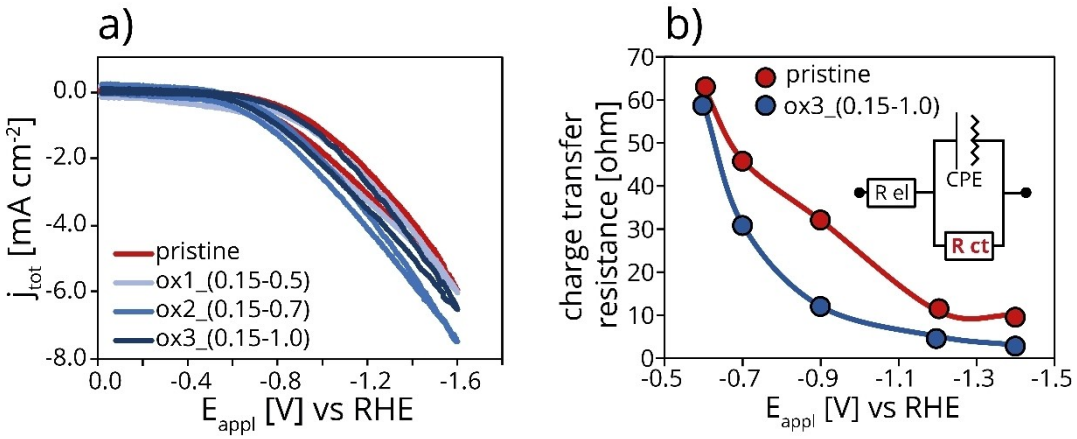

Figure 4. a) Total current density j_{tot} produced by the pristine and the oxide derived nanowires as a function of the applied potential E_{appl}, corrected for the electrolyte resistance. The measurement was performed in 0.1 M $KHCO_3$ with 10 mV s^{-1} scan rate. b) Charge transfer resistance as a function of the applied potential, measured by impedance spectroscopy in the range between 100 kHz and 1 Hz. The inset shows the equivalent circuit used to fit the impedance data (R_{el} = electrolyte resistance; CPE = constant phase element; R_{ct} = charge transfer resistance).

displaying a 2.7 times larger resistance compared to the OD-sample. These results suggest that the defective surface of OD-silver catalysts was electrochemically more active than the pristine wires, and promoted the electron transfer to either CO_2 or H_2O/H^+.

To evaluate the selectivity of the process and separate the individual contributions of the different products to the total current density, the geometric partial current densities were calculated for both pristine and OD-catalysts. This analysis was based on chronoamperometry measurements, coupled with GC analysis of the reaction products, which gives the Faradaic efficiencies (selectivity) (Figure S6). CO was the only product formed from CO_2 while H_2, formed both over carbon and silver, is the competitive product. Figure 5a clearly demonstrates that the OD-nanowires were more selective towards CO than the pristine nanowires. The ox3 (0.15–1.0) sample produced a nearly 2-fold higher CO partial current density than the pristine sample, both at −1.2 V and −1.4 V. The pristine catalyst generated the largest H_2 partial current density. The OD-materials produced about half the amount of H_2, with no clear difference between the different OD-materials (Figure 5b). Hence, the oxidation treatment promoted the conversion of CO_2 to CO and suppressed the H_2 evolution, enhancing the selectivity of the process.

Understanding the selectivity of oxide-derived silver nanowires

To assess the key parameters influencing the selectivity of the process, the surface area-normalized selectivity of the catalysts was determined (Figure 6a). The silver surface was measured by underpotential Pb deposition (Figure S7). In the current-voltage scan, two main peaks were observed, with the first due to underpotential deposition (onset = +0.1 V vs Ag/AgCl) and the second to bulk Pb deposition (onset = −0.2 V vs Ag/AgCl). The silver surface area slightly increased after oxidation to 0.5 V (ox1 (0.15–0.5) sample), but a 16% and 44% decrease in active

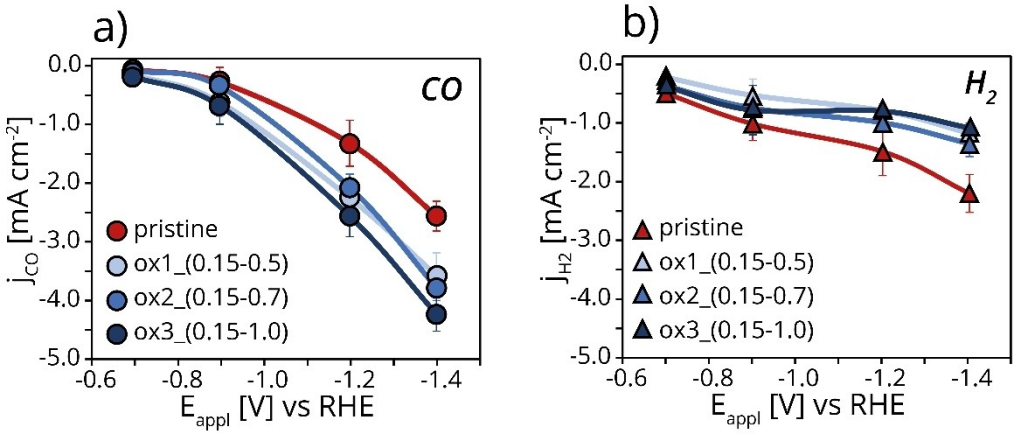

Figure 5. a) CO and b) H_2 partial current density, normalized per geometric surface area, as a function of the applied potential. The test was performed in 0.1 M $KHCO_3$ with online measurements of the gaseous products (average over 30 minutes catalysis at each potential).

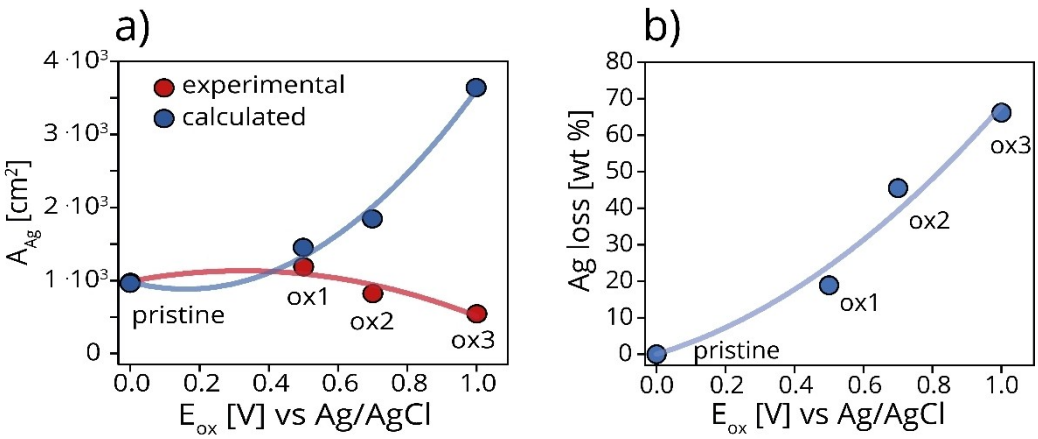

Figure 6. a) Electrochemically active silver surface area (A_{Ag}) measured by under potential lead deposition (experimental, red markers) and calculated for the theoretical situation of no silver loss (calculated, blue markers). b) silver loss as a function of the applied oxidation potential, measured by atomic absorption spectroscopy.

surface area was measured for ox2 (0.15–0.7) and ox3 (0.15–1.0) respectively, compared to the pristine nanowires (Figure 6a), red markers).

SEM already suggested that the density of silver was lower, but also showed an increased surface roughness (Figure 3) with increasing oxidation potential. Elemental analysis (Figure 6b) showed that ox3 (0.15–1.0) sample contained 66% less silver than the pristine sample. This points to the dissolution of silver oxide in the aqueous electrolyte, which results in loss of active metal and perhaps enhanced by bubble formation, possibly also some detachment of silver wires. This hypothesis is supported by previous studies, highlighting the solubility at room temperature of Ag_2O in alkaline electrolytes (forming soluble $[Ag(OH)_2]^-$).[43–45] Furthermore, the cathodic charge, obtained after the reduction of the catalysts, was lower than the anodic charge, obtained after the oxidation treatment (Figure S8). The low magnification SEM overview images of the electrodes (Figure 7), indeed show that the silver coverage (white areas) of the carbon substrate (dark areas) decreased by increasing the oxidation potential. Therefore, upon oxidation the nanowires experienced two phenomena: (I) an increase in surface roughness leading to increased surface area and (II) a loss of active metal, decreasing the metal surface area. Furthermore, we determined which surface area would be expected if the surface roughened, but no silver would have been lost by dissolution (calculated surface area, Figure 6a, blue markers) based on the specific surface area for each sample after the experiment (cm^2_{AgUPD}/g_{AgAAS}), but assuming the original silver weight loading. Hence, if we had prevented silver leaching during the oxidation treatment, the theoretical silver surface area would have increased almost exponentially with increasing oxidation potential, based on the surface roughness increase.

Figure 8 shows the specific CO partial current density of pristine (red markers) and oxidized (blue markers) as a function of the applied potential per real Ag surface area. The pristine nanowires presented the smallest specific CO current density, with only $-47.7\ mA\ m_{Ag}^{-2}$ at -1.2 V, while ox1 (0.15–0.5) and ox2 (0.15–0.7) produced $-69.2\ mA\ m_{Ag}^{-2}$ and $-106.5\ mA\ m_{Ag}^{-2}$ at the same potential. The highest CO production density per silver area was obtained with ox3 (0.15–1.0) sample, generating a 3.7-fold increase in the CO specific current density ($-178.0\ mA\ m_{Ag}^{-2}$) compared to the pristine nanowires. A similar trend was observed at -1.4 V, with ox3 (0.15–1.0)

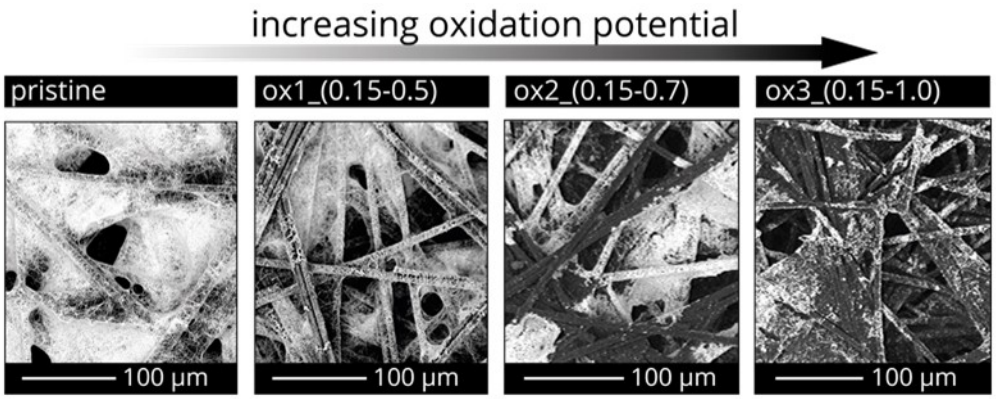

Figure 7. Low magnification SEM images of the carbon supported silver nanowires catalysts.

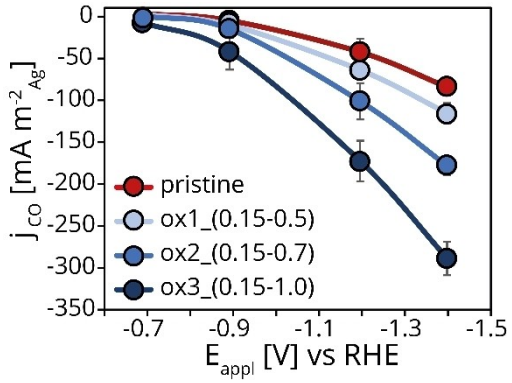

Figure 8. CO partial current density, normalized by silver electrochemically active surface area, as a function of the applied potential.

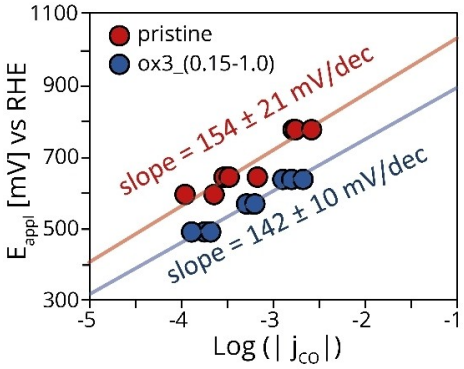

Figure 9. Tafel plot related to CO formation, measured during chronoamperometry, for both the pristine (red marker) and ox3 (0.15–1.0) samples. The error on the slope is calculated using 95% confidence level.

generating −294.2 mA m_{Ag}^{-2} and outperforming the ox2 (0.15–0.7), ox1 (0.15–0.5) and pristine catalysts, which produced only −183.6 mA m_{Ag}^{-2}, −120.8 mA m_{Ag}^{-2}, and −89.4 mA m_{Ag}^{-2}, respectively. These catalytic data demonstrates that the oxidation process significantly steered the intrinsic selectivity of the catalysts towards CO. The enhancement in specific CO partial current density reflects an improved intrinsic selectivity of the catalysts, as it does not depend on the active metal surface area.

To better understand the selectivity enhancement, we analyzed the rate determining step of the process, to determine if the change in selectivity is related to a change in the reaction pathway. We selected the pristine and the ox3 (0.15–1.0) samples for this analysis, as they showed the largest difference in selectivity.

The slope of the Tafel plot gives information about the nature of the rate-determining step of an electrochemical reaction. For the CO_2RR, the Tafel slope is 118 mV/dec if the formation of $*COO^-$ intermediate is rate limiting, due to a slow first electron transfer to CO_2. On the contrary, the Tafel slope is 59 mV/dec if the first electron transfer is fast and not limiting the reaction. This hypothesis is valid if it is assumed that the first electron transfer to CO_2 precedes the proton transfer to $*COO^-$ first reaction intermediate (uncoupled electron and proton transfer mechanism) (Figure S9).[46,25] The pristine (red markers) and ox3 (0.15–1.0) (blue markers) sample gave a Tafel slope of 154 ± 21 mV/dec and 142 ± 10 mV/dec respectively (Figure 9). Although the experimental values are higher than the theoretical value, possibly due to a slight influence of mass transfer limitations, the rather high and similar values of the Tafel slope suggest that the rate determining step for both catalysts is the first electron transfer to CO_2.

Electrocatalytic stability

As the catalysts' stability over time is a key factor for future application of electrocatalytic materials, we also investigated the stability of the catalysts by repeating three times a cycle of eight different potentials for a total of 12 hours. Figure 10a and 10b show the total geometric current density and the stability test potentials as a function of time for pristine and ox3 (0.15–1.0), respectively. At the three lowest potentials (i.e. −0.3 V, −0.4 V and −0.5 V), neither of the catalysts generated gaseous products above the GC detection limit (5 ppm for both H_2 and CO). From −0.7 V downwards, both catalysts showed an increasingly larger current density and product formation. Both pristine and OD-nanowires showed stable and reproducible current densities at low overpotentials, until −1.2 V. At larger overpotential (−1.4 V), for both ox3 (0.15–1.0) and pristine samples the current density gradually increased with time.

The partial current densities were rather stable over three cycles, as were the Faradaic efficiencies of the products (Figure S10). A small increase over cycles both in CO and H_2 partial current was measured for both pristine (Figure 10c) and ox3 (0.15–1.0) (Figure 10d) catalysts. These inspiring catalytic results from the Ag nanowires open the possibility for further studies on more industrially oriented set ups and devices such as in gas diffusion electrodes and flow cells.

These results clearly showed that the oxidation treatment on silver nanowires remarkably boosted the catalytic performance of the silver catalysts. Furthermore, it is evident that the harsher the oxidation treatment, the larger the CO partial current density per unit of silver area. The electrokinetic analysis (Tafel plot) suggested that no significant change in the reaction pathway or rate determining step occurred after oxidation. Nevertheless, the dramatic enhancement in selectivity for the oxide-derived nanowires points to the formation of new and more selective active sites for CO_2RR. It is likely that subsurface oxygen, stable during catalysis but difficult to detect even with surface techniques, promoted the reduction of CO_2 to CO by helping the stabilization of the first reaction intermediate ($*COO^-$), as previously suggested by the group of Smith.[32] Another possible explanation for the change in selectivity implies that the local pH, at the surface of the oxide-derived samples, is higher than the pH at the surface of pristine nanowires, due to the high surface roughness deriving from the oxidation treatment. High surface roughness limits the diffusion of the buffer electrolyte to the surface of the electrocatalyst, thus affecting the neutralization/back diffusion of OH^- deriving

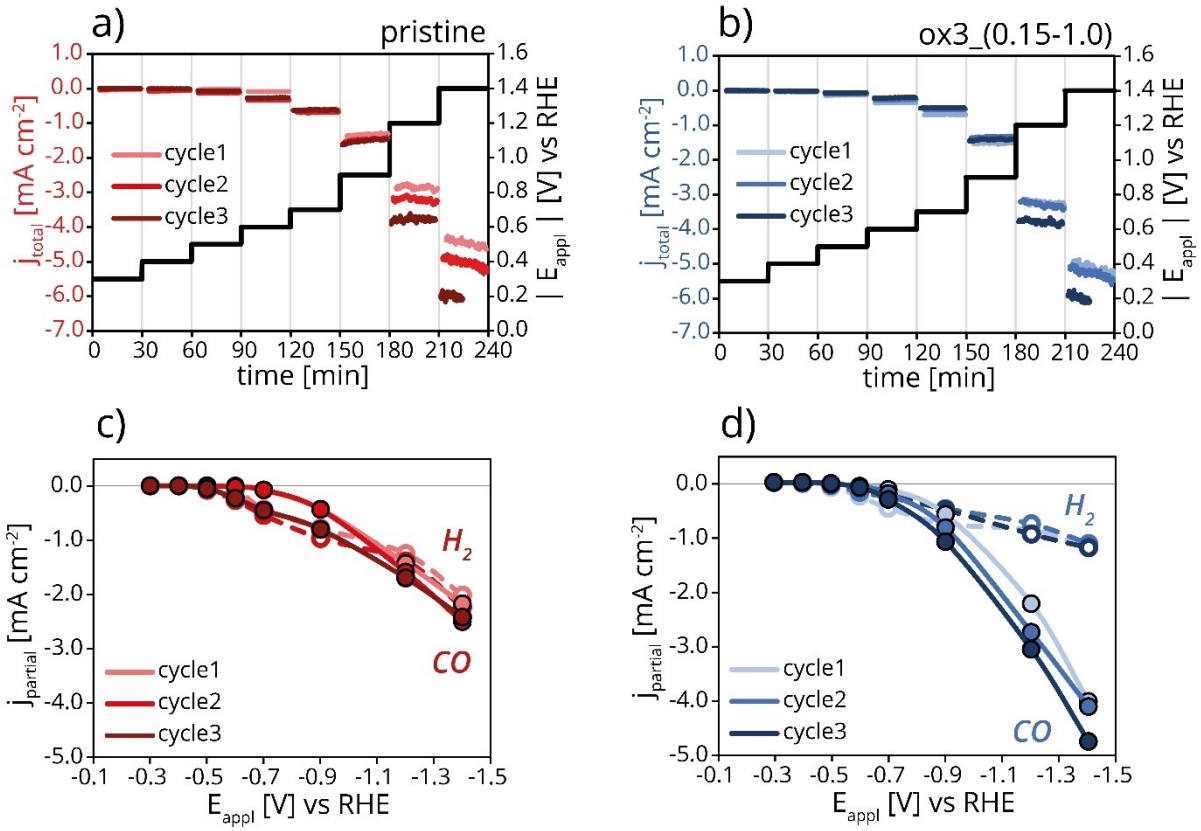

Figure 10. Chronoamperometry stability test performed over three cycles, for both a) pristine and b) ox3 (0.15–1.0) samples. CO (full marker) and H_2 (empty marker) geometric partial current density as a function of the applied potential over three potential cycles (chronoamperometry, hold time = 30 min per potential) for both c) pristine and d) ox3 (0.15–1.0) samples.

from both the HER and CO_2RR, hence affecting the reaction selectivity.[11,47] However, this explanation seems less probable, as a drastic improvement in CO FE (Figure S12) and partial current density (Figure 10c) would have been expected for the pristine nanowires after the first potential cycle during the stability tests, if the local pH would have increased. On the contrary, pristine nanowires seem to behave similarly to ox3 (0.15–1.0) sample over multiple potential cycles, hence suggesting the presence of intrinsically different active sites on the oxide-derived sample.

Conclusions

In this work, controlled electrochemical oxidation was applied to silver nanowires (aspect ratio = 160), synthesized via the polyol method. By carefully selecting the final potential during the oxidation treatment (linear sweep voltammetry), we obtained samples with different compositions, ranging from Ag^0 in the pristine nanowires to 66% AgO and 34% Ag_2O for ox3 (0.15–1.0), oxidized to 1.0 V vs Ag/AgCl. Furthermore, we systematically followed the evolution of the nanowire morphology after the oxidation and reduction process. Hence, we showed that harsher oxidation conditions (more positive applied potentials) not only generated more roughness, but also contributed to active metal loading loss. Nevertheless, the oxide-derived nanowires greatly outperformed the pristine nanowires, with ox3 (0.15–1.0) producing 3.7-fold increase in Ag surface area-normalised CO current density compared to the as-synthesized electrode. No significant difference in the rate determining step of the reaction emerged from the Tafel plot analysis. It is likely that the improvement in CO selectivity for the oxide-derived nanowires is related to the formation of new active sites (subsurface oxygen species). This work shows that a controlled oxidation treatment can be applied to well defined and CO selective silver nanostructures, and still generate an improvement in the catalytic performance, by further steering the selectivity towards CO.

Experimental Section

Synthesis of pristine silver nanowires

The pristine silver nanowires were synthesized via the polyol method.[38] The glassware (a 25 mL three-neck flask) was cleaned with concentrated nitric acid (65% wt/wt) for 1 hour. 0.34 g of poly-(vinyl)-pyrrolidone (PVP; 40 000 mol wt; Sigma–Aldrich) was dissolved in 20 mL of ethylene glycol (EG; >99%; Sigma–Aldrich) and heated to 160 °C under stirring. After complete dissolution of the PVP, 25 mg of freshly prepared AgCl was added to the solution (section 2.3). At 160 °C and in the presence of oxygen, ethylene glycol was partially oxidized to glycol aldehyde, which acted as

reducing agent for Ag^+ to Ag^0.[48] The Cl^- enabled the selective oxidative etching of the polycrystalline silver seeds, preserving the (100) and (111) crystal planes (decahedral seeds). After three minutes, 110 mg of $AgNO_3$ (99%; Sigma–Aldrich) was added to the flask, allowing the uniaxial elongation of the silver nanowires. After 24 minutes, the reaction mixture was cooled down to room temperature.

The suspension was centrifuged three times at 6000 rpm for 30 minutes in methanol (>99.9%; Sigma–Aldrich), and the solvent was decanted to remove impurities. Finally, the precipitate was dispersed in methanol and stored in the dark, in a vial sealed with Teflon tape to avoid solvent evaporation. A fraction of the as-synthesized silver nanowires was drop casted on top of a carbon paper electrode (sample name: pristine), while part of the batch was subjected to the oxidation/reduction procedure (sample name: oxY (0.15–Z), where Y = 1, 2 or 3, with 1 indicating the least oxidized sample, and 3 the most oxidized sample; Z represents the final oxidation potential). For instance ox1 (0.15–0.5) stands for OD-nanowires oxidized by applying a potential sweep between +0.15 V and +0.5 V vs Ag/AgCl.

Synthesis of fresh AgCl

Silver chloride (AgCl) is a photosensitive compound. Therefore, the use of freshly made silver chloride for the synthesis of silver nanowires is necessary to avoid the formation of metallic silver by photoreduction of silver chloride in stock batches. The synthesis of AgCl was performed in a vial wrapped in aluminum foil, to avoid direct contact with light, via a one-step procedure. A 0.5 M solution of silver nitrate was mixed with a 1 M solution of sodium chloride, while stirring at 500 rpm for 5 minutes. After the addition of sodium chloride, silver chloride flocculates immediately. The precipitate was separated from the supernatant, washed once with ultrapure water and dried under vacuum.

Synthesis of oxide derived silver nanowires

To oxidize and reduce the silver nanowires, we used a custom-made oxidation-reduction holder, (Figure S11). After drop casting 0.3 $mg_{Ag}\,cm^{-2}$ onto a carbon paper substrate, we placed the carbon cloth on top of a glassy carbon disc, in contact with a copper wire connected to the external electric circuit. The holder allows to protect one side of the carbon paper, and at the same time guarantees optimal electrical contact between the catalyst and the electrical source. To oxidize in a controlled fashion the silver electrodes, we chose linear sweep voltammetry (LSV, scan rate = 10 $mV\,s^{-1}$) performed in 0.2 M NaOH (pH = 13) in a beaker, using a three-electrode configuration, with Ag/AgCl as reference and a Pt wire as counter electrode. The reduction of the oxidized electrode was performed via LSV (scan rate = 10 $mV\,s^{-1}$) in 0.1 M $KHCO_3$ in a beaker, prior to starting the catalytic tests, to avoid perturbations during the CO_2RR.

Characterization

Transmission electron microscopy (TEM) images of the pristine nanowires were acquired using a Thermo Fischer Scientific Tecnai20 microscope, operated at 200 kV. The holey carbon 200 mesh copper grids were prepared by drop casting the silver nanowires colloidal solution directly on the grid and dried at room temperature. The silver nanowires average diameter and length was determined by analyzing 10 different TEM images and around 97 nanowires. The average diameter (or length) was calculated as follow:

$$d_{avrg}\left(or\ l_{avrg}\right) = \frac{\sum_i^n d_n\ (or\ l_n)}{N},$$

where d_n *(or* l_n*)* is the diameter (or length) of particle n, and N is the total number of particles counted. Scanning electron microscopy (SEM) images were acquired on a FEI PhenomProX from Phenom-world at 10 kV, imaging using the backscatter detector. High resolution SEM images were acquired using a FEI Helios G3 UC microscope, operated at 10 kV. Sticky carbon tape was used to attach the electrodes on the sample holder.

X-ray diffraction measurements were performed on a Bruker D2 Phaser, equipped with a Co K_α X-ray source with a wavelength of 1.79026 Å. Rietveld refinement analysis was performed using MAUD software, considering R_{wp} and χ^2 as indicators for the quality of the fitting.[49] The XPS data were collected at TU Eindhoven by using ThermoFischer Thermo Scientific K-Alpha X-ray Photoelectron Spectrometer System, with an Al source (Kα monochromatic radiation, 1486.6 eV). The deconvolution and quantification of the silver peaks was achieved using CasaXPS and Origin. The carbon peak at 284.84 eV was used as a calibration for energy. UV-vis measurements were performed on Agilent Technologies Cary 60 UV-Vis, and they were used to monitor the purity of the silver nanowires during the synthesis. The transmission was measured using a single beam mode and used to calculate the absorbance. The solvent absorbance was subtracted from that of the Ag NWs colloidal suspension. The sample (Ag NWs in MeOH) was diluted 100 times with Millli-Q water.

To determine the silver metal weight loading on the carbon paper support, the concentration of silver in the colloidal solution was measured by Inductively Coupled Plasma (ICP) on PerkinElmer Optima 8300 Optical Emission Spectrometer. The precise amount of silver was deposited on the carbon paper by using a Finn pipet. The silver loss during the oxidation and reduction procedure was quantified by atomic absorption spectroscopy on a ContrAA 700 AAS instrument. The electrochemical surface area measurements were performed using the underpotential lead deposition method in 0.01 M $Pb(NO_3)_2$ (99.999%; Sigma–Aldrich) + 0.01 M HNO_3 (65% wt/wt; Sigma–Aldrich), assuming $1.67\times10^{-3}\,cm^2\,\mu C^{-1}$ and a scan rate of 10 $mV\,s^{-1}$.[17]

Electrochemical measurements

A three-electrode custom-built H-type electrochemical cell, made of polymethylmethacrylate, was used for the electrocatalytic experiments (Figure S12). The cathodic and anodic compartments (electrolyte volume = 15 mL/each; headspace volume = 3 mL/each) were divided by a Nafion 117 membrane (Ion Power). The CO_2 saturated catholyte was purged with 20 $mL\,min^{-1}$ CO_2 (Linde, purity 5.2), while the anolyte was stirred by bubbling Ar (20 $mL\,min^{-1}$). The working electrode was composed of a glassy carbon disc (HTW-Germany), in contact with the carbon paper disc (TGP-H-060, Toray) on top of which we deposited the silver nanowires. Onto the carbon paper (total electrode area = 4.9 cm^2) the silver nanowires colloidal suspension was drop cast and dried overnight at room temperature. A silver weight loading of 0.3 $mg_{Ag}\,cm^{-2}$ was used for the pristine nanowires electrode, as determined by measuring the silver content via ICP. The carbon paper surface area in contact with the potassium bicarbonate (>99%; Sigma–Aldrich) electrolyte (0.1 M; pH = 6.8) was 3.8 cm^2. We used an Ag/AgCl (3 M KCl) reference electrode (Metrohm) and a 3.8 cm^2 Pt disc (99.5%; Goodfellow) as counter electrode. The electrochemical measurements were performed using a Parstat MultiChannel potentiostat/galvanostat, with a MultiChannel −1000 AC/DC channel for electrochemical impedance measurements.

The electrocatalytic activity was measured both with chronoamperometry and with cyclic voltammetry, corrected for the uncompensated potential measured by impedance spectroscopy (electrolyte resistance). The results were confirmed by chronoamperometry measurements at different potentials for 30 minutes. The gaseous products were analyzed online by gas chromatography, using Global Analysis Solutions Microcompact GC 4.0 machine from InterScience, already described in a previous work.[50]

Nuclear magnetic resonance spectra of liquid products were taken at 298 K on a Varian MRF400 spectrometer. Only traces of formate were detected in the liquid phase, therefore mainly CO and H_2 contributed to the selectivity of the process. The selectivity of the process was defined by the Faradaic efficiency (FE), calculated as:

$$FE = \frac{(n^*F\ ^*mol)}{i_{tot}{}^*t},$$

where n is the moles of electrons per mole of product ($mol_P\,mol_{e^-}^{-1}$), F is the Faraday constant (C mol_{e^-}), *mol* is the moles of products formed (mol_P), i is the total current ($C\,s^{-1}$), and t the analysis time (s). The partial current density defines the individual contribution of the reaction products to the total current density. This parameter was calculated as the product of the total current density and the FE. The impedance measurements were performed on the Parstat MultiChannel −1000 channel of PARSTAT potentiostat, using a frequency range from 0.1 Hz to 100 kHz. The impedance measurements for the charge transfer resistance quantification were performed at the indicated potentials, right after the chronoamperometry measurement at the same potential. Before fitting the Nyquist plots with the equivalent circuit described later, we performed a Kramers-Kroning test on the raw data. Impedance data were analyzed via EQC software,[51] following the data validation described in previous work.[52] All fits performed resulted in $\chi^2 < 10^{-3}$.

Acknowledgements

Francesco Mattarozzi, Claudia Keijzer and Rim van de Poll were funded by the Dutch Research Council (NWO), via the Advanced Research Center Chemical Building Blocks Consortium (ARC-CBBC) in collaboration with Shell Global Solutions International B.V. Stephan Jonker is acknowledged for the precious help with the atomic absorption spectroscopy measurements. Matteo Parente is acknowledged for the fruitful discussions regarding the synthesis of the pristine silver nanowires. Valerio Gulino acknowledges funding from RELEASE (project number: 17621). Nienke Visser is acknowledged for the TEM images of the pristine nanowires. Matt Peerlings and Maaike van Ittersum are acknowledged for the useful discussions related to the electrochemical results. Jan Willem de Rijk is acknowledged for the technical support, helping both with the cell design and the preparation of the catalytic set-up during this project.

Conflict of Interests

The authors declare no conflict of interest.

Data Availability Statement

The data that support the findings of this study are available from the corresponding author upon reasonable request.

Keywords: silver nanowires · oxide-derived metal · CO_2 reduction · charge transfer resistance · CO production

[1] H. Chen, T. N. Cong, W. Yang, C. Tan, Y. Li, Y. Ding, *Prog. Nat. Sci.* **2009**, *19*, 291–312.
[2] T. Hatsukade, K. P. Kuhl, E. R. Cave, D. N. Abram, T. F. Jaramillo, *Phys. Chem. Chem. Phys.* **2014**, *16*, 13814–13819.
[3] P. Atkins, J. de Paula, *Physical Chemistry*, W. H. Freeman, New York, **2006**.
[4] Y. Hori, in *Mod. Asp. Electrochem.*, Springer New York, New York, NY, **2008**, 89–189.
[5] R. Zhang, W. Lv, G. Li, M. A. Mezaal, L. Lei, *RSC Adv.* **2015**, *5*, 68662–68667.
[6] R. Kas, K. Yang, D. Bohra, R. Kortlever, T. Burdyny, W. A. Smith, *Chem. Sci.* **2020**, *11*, 1738–1749.
[7] D. Bogdanov, M. Ram, A. Aghahosseini, A. Gulagi, A. S. Oyewo, M. Child, U. Caldera, K. Sadovskaia, J. Farfan, L. De Souza Noel Simas Barbosa, M. Fasihi, S. Khalili, T. Traber, C. Breyer, *Energy* **2021**, *227*, 120467.
[8] F. P. García de Arquer, C. T. Dinh, A. Ozden, J. Wicks, C. McCallum, A. R. Kirmani, D. H. Nam, C. Gabardo, A. Seifitokaldani, X. Wang, Y. C. Li, F. Li, J. Edwards, L. J. Richter, S. J. Thorpe, D. Sinton, E. H. Sargent, *Science* **2020**, *367*, 661–666.
[9] X. Chen, J. Chen, N. M. Alghoraibi, D. A. Henckel, R. Zhang, U. O. Nwabara, K. E. Madsen, P. J. A. Kenis, S. C. Zimmerman, A. A. Gewirth, *Nat. Catal.* **2021**, *4*, 20–27.
[10] Y. Zhou, A. J. Martín, F. Dattila, S. Xi, N. López, J. Pérez-Ramírez, B. S. Yeo, *Nat. Catal.* **2022**, *5*, 545–554.
[11] A. Goyal, G. Marcandalli, V. A. Mints, M. T. M. Koper, *J. Am. Chem. Soc.* **2020**, *142*, 4154–4161.
[12] Y. Hori, *Handbook of Fuel Cell,* John Wiley & Sons **2010**.
[13] G. J. Sunley, D. J. Watson, *Catal. Today* **2000**, *58*, 293–307.
[14] H. Schulz, *Appl. Catal. A* **1999**, *186*, 3–12.
[15] D. Sun, X. Xu, Y. Qin, S. P. Jiang, Z. Shao, *ChemSusChem* **2020**, *13*, 39–58.
[16] J. T. Feaster, C. Shi, E. R. Cave, T. Hatsukade, D. N. Abram, K. P. Kuhl, C. Hahn, J. K. Nørskov, T. F. Jaramillo, *ACS Catal.* **2017**, *7*, 4822–4827.
[17] C. Kim, H. S. Jeon, T. Eom, M. S. Jee, H. Kim, C. M. Friend, B. K. Min, Y. J. Hwang, *J. Am. Chem. Soc.* **2015**, *137*, 13844–13850.
[18] Y. Zhang, L. Liu, L. Shi, T. Yang, D. Niu, S. Hu, X. Zhang, *Electrochim. Acta* **2019**, *313*, 561–569.
[19] L. Wei, H. Li, J. Chen, Z. Yuan, Q. Huang, X. Liao, G. Henkelman, Y. Chen, *ACS Catal.* **2020**, *10*, 1444–1453.
[20] L. Zeng, J. Shi, H. Chen, C. Lin, *Energies* **2021**, *14*, 2840–2850.
[21] J. Ge, J. Long, Z. Sun, H. Feng, J. Hu, S. W. Koh, Q. Yu, J. Xiao, H. Li, *ACS Appl. Energ. Mater.* **2019**, *2*, 6163–6169.
[22] C. Luan, Y. Shao, Q. Lu, S. Gao, K. Huang, H. Wu, K. Yao, *ACS Appl. Mater. Interfaces* **2018**, *10*, 17950–17956.
[23] S. Liu, X. Z. Wang, H. Tao, T. Li, Q. Liu, Z. Xu, X. Z. Fu, J. L. Luo, *Nano Energy* **2018**, *45*, 456–462.
[24] L. Hu, Y. Zhang, W. Han, *New J. Chem.* **2019**, *43*, 3269–3272.
[25] Y. Chen, C. W. Li, M. W. Kanan, *J. Am. Chem. Soc.* **2012**, *134*, 19969–19972.
[26] J. J. Velasco-Vélez, C. H. Chuang, D. Gao, Q. Zhu, D. Ivanov, H. S. Jeon, R. Arrigo, R. V. Mom, E. Stotz, H. L. Wu, T. E. Jones, B. Roldan Cuenya, A. Knop-Gericke, R. Schlögl, *ACS Catal.* **2020**, *10*, 11510–11518.
[27] Z. Qi, J. Biener, M. Biener, *ACS Appl. Energ. Mater.* **2019**, *2*, 7717–7721.
[28] C. W. Li, M. W. Kanan, *J. Am. Chem. Soc.* **2012**, *134*, 7231–7234.
[29] D. Ren, Y. Deng, A. D. Handoko, C. S. Chen, S. Malkhandi, B. S. Yeo, *ACS Catal.* **2015**, *5*, 2814–2821.
[30] M. Ma, B. J. Trześniewski, J. Xie, W. A. Smith, *Angew. Chem. Int. Ed.* **2016**, *55*, 9748–9752.
[31] K. Jiang, P. Kharel, Y. Peng, M. K. Gangishetty, H. Y. G. Lin, E. Stavitski, K. Attenkofer, H. Wang, *ACS Sustainable Chem. Eng.* **2017**, *5*, 8529–8534.
[32] N. J. Firet, M. A. Blommaert, T. Burdyny, A. Venugopal, D. Bohra, A. Longo, W. A. Smith, *J. Mater. Chem. A* **2019**, *7*, 2597–2607.
[33] Y. Ye, H. Yang, J. Qian, H. Su, K. J. Lee, T. Cheng, H. Xiao, J. Yano, W. A. Goddard, E. J. Crumlin, *Nat. Commun.* **2019**, *10*, 1–9.

[34] H. Mistry, Y. Choi, A. Bagger, F. Scholten, C. S. Bonifacio, I. Sinev, N. J. Divins, I. Zegkinoglou, H. S. Jeon, K. Kisslinger, E. A. Stach, J. C. Yang, J. Rossmeisl, B. Roldan Cuenya, *Angew. Chem.* **2017**, *129*, 11552–11556.
[35] X. Wu, Y. Guo, Z. Sun, F. Xie, D. Guan, J. Dai, F. Yu, Z. Hu, Y. C. Huang, C. W. Pao, J. L. Chen, W. Zhou, Z. Shao, *Nat. Commun.* **2021**, *12*, 1–11.
[36] W. A. Al-Saidi, H. Feng, K. A. Fichthorn, *Nano Lett.* **2012**, *12*, 997–1001.
[37] J. Zeng, Y. Zheng, M. Rycenga, J. Tao, Z. Y. Li, Q. Zhang, Y. Zhu, Y. Xia, *J. Am. Chem. Soc.* **2010**, *132*, 8552–8553.
[38] M. Parente, M. Van Helvert, R. F. Hamans, R. Verbroekken, R. Sinha, A. Bieberle-Hütter, A. Baldi, *Nano Lett.* **2020**, *20*, 5759–5764.
[39] A. Al-Sarraj, K. M. Saoud, A. Elmel, S. Mansour, Y. Haik, *SN Appl. Sci.* **2021**, *3*, 1–13.
[40] T. U. Hur, W. S. Chung, *J. Electrochem. Soc.* **2005**, *152*, A996.
[41] D. Lützenkirchen-Hecht, H. H. Strehblow, *Surf. Interface Anal.* **2009**, *41*, 820–829.
[42] J. E. B. Randles, *Discuss. Faraday Soc.* **1947**, *1*, 11–19.
[43] H. L. Johnston, F. Cuta, *J. Am. Chem. Soc.* **1933**, *55*, 2311–2325.
[44] S. S. Abd El Rehim, H. H. Hassan, M. A. M. Ibrahim, M. A. Amin, *Monatsh. Chem.* **1998**, *129*, 1103–1117.
[45] D. B. Gibbs, B. Rao, R. A. Griffin, M. J. Dignam, *J. Electrochem. Soc.* **1975**, *122*, 1167–1174.
[46] M. Dunwell, W. Luc, Y. Yan, F. Jiao, B. Xu, *ACS Catal.* **2018**, *8*, 8121–8129.
[47] Y. Yoon, A. S. Hall, Y. Surendranath, *Angew. Chem. Int. Ed.* **2016**, *55*, 15282–15286.
[48] S. E. Skrabalak, B. J. Wiley, M. Kim, E. V. Formo, Y. Xia, *Nano Lett.* **2008**, *8*, 2077–2081.
[49] H. R. Lutterotti, L. Matthies, S. Wenk, *MAUD: A Friendly Java Program for Material Analysis Using Diffraction* **1999**, 14–15.
[50] F. Mattarozzi, N. Visser, J. W. de Rijk, P. Ngene, P. de Jongh, *Eur. J. Inorg. Chem.* **2022**, 10.1002/ejic.202200365.
[51] B. Boukamp, *Solid State Ionics* **2004**, *169*, 65–73.
[52] B. Boukamp, *Solid State Ionics* **1986**, *18-19*, 136–140.

Manuscript received: June 26, 2023
Revised manuscript received: October 3, 2023
Accepted manuscript online: October 5, 2023
Version of record online: October 30, 2023